The relation between dissipation and memory in two-fluid displacements in disordered media

Ran Holtzman[1], Marco Dentz[2], Ramon Planet[3,4], and Jordi Ortín[3,4]

[1]Coventry University, Centre for Fluid and Complex Systems, Coventry, United Kingdom
[2]Spanish National Research Council (IDAEA-CSIC), Barcelona, Spain
[3]Departament de Física de la Matèria Condensada, Universitat de Barcelona, Barcelona, Spain
[4]Institute of Complex Systems, Universitat de Barcelona Barcelona, Spain

Key Points:

- Rigorous account of the microscopic physics allows to compute the energy dissipated between consecutive two-phase configurations
- We link the microscopic origins of hysteresis and dissipation to the macroscopic pressure-saturation behavior
- Quasistatic pressure-driven experiments point to a secondary contribution of viscous dissipation during Haines jumps

Abstract

We show that the return-point memory of cyclic macroscopic trajectories enables the derivation of a thermodynamic framework for quasistatically driven dissipative systems with multiple metastable states. We use this framework to sort out and quantify the energy dissipated in quasistatic fluid-fluid displacements in disordered media. Numerical computations of imbibition–drainage cycles in a quasi-2D medium with gap thickness modulations (imperfect Hele-Shaw cell) show that energy dissipation in quasistatic displacements is due to abrupt changes in the fluid-fluid configuration between consecutive metastable states (Haines jumps), and its dependence on microstructure and gravity. The relative importance of viscous dissipation is deduced from comparison with quasistatic experiments.

Plain Language Summary

Fluid flow into a porous material filled with another is not only an everyday process (gardening, stains in fabrics, or printing) but is also a key process affecting the water cycle, contamination in soils and storage of energy or hazardous waste in the subsurface. These flows are controlled by the energy of the fluids, and its dissipation during their advancement, making the knowledge of energy dissipation crucial to our ability to predict these phenomena. However, to date there is no rigorous way to evaluate this energy. This paper describes a novel method that overcomes this challenge, explaining how the properties of the medium affect dissipation and showing why even for very slow flows the viscous energy (that is related to rapid fluid motion) still makes a difference.

1 Introduction

Energy dissipation is unavoidable in fluid-fluid displacements through disordered media even in the ideal limit of quasistatic driving, because displacements in heterogeneous media take place inherently out of equilibrium. Configurational changes in the passage from one metastable equilibrium state to another give rise to energy losses. As a result the macroscopic variables defining the system response exhibit hysteresis upon cyclic solicitations (Bertotti & Mayergoyz, 2006). This scenario is generic to other driven disordered systems such as elastic lines, disordered magnets, and granular packings (Wiese, 2022).

Corresponding author: Ran Holtzman, ran.holtzman@coventry.ac.uk

Memory is a striking property of quasistatically driven disordered systems (Keim et al., 2019; Pashine et al., 2019; Shohat & Lahini, 2023). In the context of fluid systems in disordered media, memory shows up not only in two-phase displacements in porous and fractured media (Albers, 2014; Cueto-Felgueroso & Juanes, 2016; Holtzman et al., 2020) but also in capillary condensation of gases in nanoporous solids (Kierlik et al., 2001; Valiullin et al., 2006; Alvine et al., 2006; Hiratsuka et al., 2016). This is important for the rise of sap in plants (Holbrook & Zwieniecki, 2008), infiltration into soils (Sahimi, 2011), efficiency of energy conversion in fuel cells (Tranter et al., 2018), and several other natural and engineered processes. Despite extensive work on the thermodynamics of multiphase flows in heterogeneous media (Hu et al., 2018; McClure et al., 2021; Bedeaux & Kjelstrup, 2022; Primkulov et al., 2020; Måløy et al., 2021), the link between memory and dissipation is still missing. The latter has recently become the focus of research in driven disordered systems in general (Shohat & Lahini, 2023).

Here we show that the return-point memory of quasistatic hysteresis cycles can be used to establish a rigorous thermodynamic (macroscopic) framework to sort out and evaluate the energy dissipated in the passage between metastable equilibria. This framework provides a link between microscale quantities (microscopic quenched disorder, metastable equilibrium configurations) and the upscaled macroscopic trajectories and energy dissipation. The procedure is generic; here we apply it to a model of fluid-fluid displacements in an open fracture (an imperfect Hele-Shaw cell) where the microscopic physical mechanisms of surface tension and capillarity lead to macroscopic pressure-saturation (PS) trajectories exhibiting the complex behavior of hysteresis and return-point memory (RPM).

2 Energy balance

2.1 Generic formulation for fluid-fluid displacements

Energy conservation ensures that between consecutive metastable equilibria the mechanical work invested in driving the fluids is partially stored as internal energy of the multiphase system configuration, and partially dissipated. Thus, for an infinitesimal change in wetting-phase saturation (corresponding to a volume change dV_w), the energy balance

$$đW = dU - đ\Psi \tag{1}$$

applies, where we have adopted the convention that $đW > 0$ is the external mechanical work performed on the system to drive the displacing fluid ($đW < 0$ if extracted; the sign depends on the external force and direction of advancement), $dU > 0$ is the increase in internal energy of the two-fluid configuration, and $đ\Psi \leq 0$ is the amount of energy dissipated. The terms in Eq. (1) refer to changes between two consecutive metastable equilibria, and $đ$ denotes differentials of magnitudes that are not state functions (i.e. that depend on the path in the PS space). $đ\Psi$ could be cast in terms of entropy production, but thermal fluctuations here are insufficient to bring the system over the large energy barriers between neighboring equilibrium configurations.

We consider first a generic scenario in which a fluid is injected at one side (inlet) of a disordered domain and displaces a second fluid. A specific example is the system shown in Fig. 1. For a given disorder realization, the total energy of the system (its Hamiltonian $\mathcal{H}$) depends simultaneously on the interfacial configuration $\{\xi\}$, e.g. the location and shape of the fluid-fluid interface (a microscopic feature), and the applied (macroscopic) pressure P on the fluid at the inlet; thus, every equilibrium state is defined by $\{\xi\}$ and P. To obtain U and W, we split the Hamiltonian through the Legendre transformation $\mathcal{H} = U - PV_w$, where V_w is the volume of the wetting phase in the domain (saturation times domain volume). In contrast with $\mathcal{H}$, the internal energy U of the multiphase configuration depends only on the set of variables $\{\xi\}$ and not on the sequence of driving pressures P. The crucial point comes now: if the RPM property holds, the configuration $\{\xi\}$ is exactly recovered in a cyclic excursion of P. Thus, $U = U(\{\xi\})$ also returns to its original value in a cyclic excursion, making it a true state function. We note that the internal energy of the compartment models developed by Cueto-Felgueroso and Juanes (2016) and Helland et al. (2021) is also a state function, thanks to the RPM property. In contrast, the amount of work depends on the path in the PS space,

$$đW = P\, dV_w. \tag{2}$$

This expression relies on the incompressibility of the more wetting fluid, which guarantees that the amount of fluid displaced at the boundary of the domain coincides with the change of its volume in the medium. In this convention, the sign of $đW$ depends on that of P (< 0 in tension and > 0 in compression) and dV_w (> 0 in imbibition and < 0 in drainage).

Under quasistatic driving, a trajectory in the PS space is made of consecutive displacements of two types. In *isons*, the system remains trapped in a local energy minimum while P evolves exceedingly slowly and causes a smooth evolution of V_w. In *rheons*, an abrupt change in V_w occurs at constant P. Rheons take place when the limit of metastability of a local energy minimum is reached, the minimum disappears, and the system jumps to a new minimum, in what is called a Haines jump. In the idealised case of quasistatic driving, the timescales of these two kinds of displacements are infinitely separated, such that Haines jumps are effectively instantaneous in the time scale of P. This is the prototypical framework of spatially-extended athermal systems that undergo collective rearrangements (avalanches) under quasistatic driving (Leschhorn et al., 1997; Jensen, 1998; Pruessner, 2012). The dissipation between two consecutive equilibrium configurations ($t-1$ and t) is obtained by integrating Eq. (1),

$$\Psi^{t-1\to t} = \left[U^t - U^{t-1}\right] - P^t \left[V_w^t - V_w^{t-1}\right]. \tag{3}$$

$\Psi^{t-1\to t}$ is nonzero in rheons.

Also, since U is a state function, $\oint dU = 0$ in a closed PS cycle. Integrating Eq. (3) along the cycle demonstrates that the total energy dissipated is the area encompassed within the cycle on the PS plane,

$$\Psi_{\text{cyc}} = \oint d\Psi = -\oint đW = -\oint P\, dV_w. \tag{4}$$

Furthermore, since by definition $\Psi_{\text{cyc}} \leq 0$, there is only one sense allowed for contouring the cycle: for a given V_w the drainage path occurs at lower P than the imbibition path–in agreement with experimental observations (Albers, 2014).

2.2 Model system: An imperfect Hele-Shaw cell

To gain further quantitative understanding of the microscopic mechanisms for dissipation, and enable rigorous comparison with experiments, we derive explicit expressions of W, U and Ψ for quasistatic two-fluid displacements in an imperfect Hele-Shaw cell, in the framework of the model introduced by Holtzman et al. (2020). The model considers the 2D projection of a heterogeneous Hele-Shaw cell, subjected to an effective gravity g_e in order to prevent viscous fingering during drainage (Fig. 1). Gravity also allows investigating a wider range of pressure-saturation values than for a horizontal cell, as in the absence of heterogeneity there is no equilibrium position without gravity (Holtzman et al., 2020; Ayaz et al., 2020).

Disorder is provided by fluctuations in capillary pressure at the fluid-fluid interface, corresponding to localized modulations in the gap thickness, $b(x, y)$ ("defects" forming constrictions and expansions). Fluid displacements are driven by an external pressure $P = \rho g H$ applied at the inlet, with ρ being the wetting fluid density, g the gravitational acceleration, and H the external head. The density of the second fluid is considered negligible (air).

Multiphase configurations $\{\xi\}$ in the projected 2D model correspond to metastable equilibrium interface positions, $\{h(x)\}$. For a given disorder realization, they can be resolved from the pressure balance (Holtzman et al., 2020)

$$\gamma \frac{d^2h}{dx^2} - \rho g_e h + P + p_c(x, h) = 0. \tag{5}$$

The first term is the linear approximation (considering small interface deformations, $|dh/dx| < 1$) of the in-plane contribution to the Young-Laplace pressure jump across the interface, with γ the interfacial tension; the second is the hydrostatic pressure of the wetting fluid column at position x; the third is the external forcing; and the fourth $p_c(x, y) = 2\gamma \cos\theta / b(x, y)$ is the out-of-plane contribution to the Young-Laplace pressure jump at the front position $h(x)$, with θ the apparent contact angle. Each disorder realization is defined by the microstructure $b(x, y)$. Considering mild local interface deformations we rule out the possibility of overhangs or complex processes such as snapoff.

The condition of mechanical equilibrium in Eq. (5) can also be expressed as $p_e[h(x)] = -\delta\mathcal{H}/\delta h(x) = 0$, with the Hamiltonian given by

$$\mathcal{H} = \int_0^L dx \left[\frac{\gamma}{2}\left(\frac{dh}{dx}\right)^2 + \int_0^h dy\, (\rho g_e y - P - p_c)\right]. \tag{6}$$

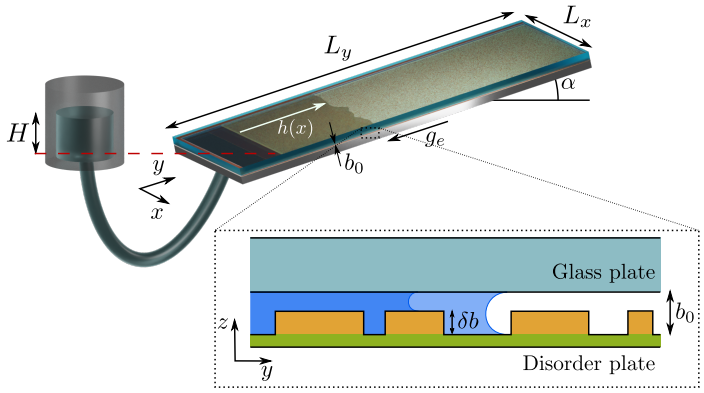

Figure 1. Schematic of the model and its experimental realization. Disorder is introduced by randomly placed "mesa defects"—sharp variations in gap thickness, $b(x,y) = b_0 \pm \delta b(x,y)$. Imbibition and drainage are driven by raising and lowering the wetting fluid reservoir, H. The cell is tilted to provide an effective gravity $g_e = g \sin\alpha$. The interface configurations $h(x)$ are recorded by a camera.

This is equivalent to the Hamiltonian of a continuous Random Field Ising Model (RFIM) where $p_c(x,y)$ plays the role of the random field (Grinstein & Ma, 1983; Ganesan & Brenner, 1998). The terms in $\mathcal{H}$ as well as W, U and Ψ in the forthcoming analysis are in units of energy per length, i.e., in our 2D model they are normalized by the average gap thickness b_0. Similarly, in 2D we use the area covered by the wetting fluid, $S_w = \int_0^L dx \int_0^{h(x)} dy$, instead of its volume V_w. Its relation to the wetting phase saturation S_w^* is given in the Supporting Information. We note that for very large thickness variations, the integrals computing the energies should be corrected to take into account these variations.

Introducing Eq. (6) into $\mathcal{H} = U - PS_w$ provides the internal energy (per unit thickness) of a given equilibrium configuration $h(x)$,

$$U = \int_0^L dx \left[\frac{\gamma}{2} \left(\frac{\partial h}{\partial x} \right)^2 + \int_0^h dy \left(\rho g_e y - p_c \right) \right]. \tag{7}$$

L is the width of the cell in the x direction. This expression of U accounts for the capillary energy of the in-plane and out-of-plane front deformations (1st and 3rd terms), and the gravitational potential energy of the wetting fluid. The work in Eq. 2 for every elementary step dS_w is $đW = P \int_0^L dx\, dh(x)$.

The internal energy U is the energy of static equilibrium configurations, when the meniscus is at rest and the energy depends only on capillary and hydrostatic forces. According to Eq. (3), the change in internal energy between two consecutive equilibrium configurations does not equate the work provided by the external driving; the difference is the energy dissipated, $\Psi^{t-1\to t}$, which in this framework is a loss of interfacial energy. This formulation does not account for viscous losses (viscosity of the fluids is not accounted for), in the expectation that they will be comparatively small in quasistatic displacements, as shown later.

3 Dissipation in avalanches and the role of system properties

Dissipation depends on the interactions between the interface and the disordered medium. Surface tension introduces correlations along the interface, and the medium spatial heterogeneities turn these correlations into complex collective behavior (Holtzman et al., 2020). Spatial interactions among multiple defects of variable properties lead to a wide range of avalanche sizes (jumps in saturation) and dissipated energies.

To exemplify these properties of energy dissipation we compare the probability density function (PDF) of the energy dissipated within individual jumps (between adjacent equilibrium configurations $t-1$ and t) normalized by the work input. We generate the disordered medium by randomly placing defects (Fig. 1) of vari-

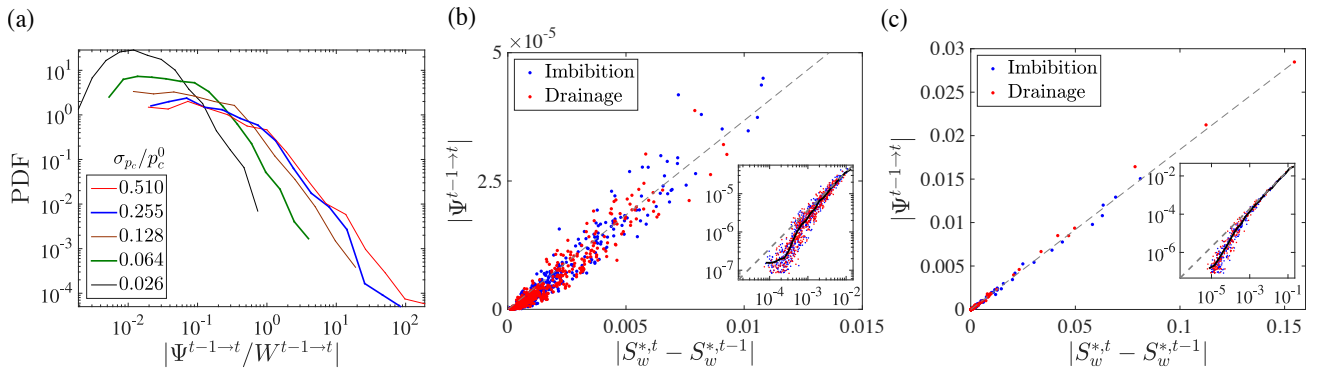

Figure 2. (a) The probability density function (PDF) of the energy dissipated in individual jumps, $\Psi^{t-1\to t}$, normalized by the work, $W^{t-1\to t}$, for systems with different widths of the defect strength distribution, σ_{p_c}. Panels (b) and (c) show the energy dissipation (in J/m) against the corresponding avalanche sizes (in terms of dimensionless saturation, $|S_w^{*,t} - S_w^{*,t-1}|$), for narrow and wide distributions, σ_{p_c}/p_c^0 of 0.026 and 0.510, respectively. The insets emphasize the larger spread of smaller values as well as their deviation from a linear relationship (dashed line); the solid black line is the conditional average.

ous strengths p_c, drawn from different distributions (here, Gaussian with standard deviation σ_{p_c} and dichotomic; see Supporting Information. To establish the role of the disorder strength, we compare media of variable width of the defect strength distribution, σ_{p_c} (keeping the spatial distribution identical; see Supporting Information). Increasing σ_{p_c}, which sets the magnitude of strongest defects, increases the magnitude of the dissipation events, stretching the PDF towards larger values (see Fig. 2a). Figure 2 also demonstrates that the energy dissipated in a single jump could greatly exceed the work invested in driving the system. This is because the energy released in an avalanche could have been stored as internal energy during many previous elementary steps. Most of the dissipation during a complete imbibition-drainage cycle therefore occurs in a handful of large events (Videos 1–2 in Supporting Information). This behavior is akin to the sudden release of energy in earthquakes (Sornette & Sornette, 1989) or granular avalanches (Denisov et al., 2016).

Another nonintuitive result is that the avalanche size (change in saturation) is not necessarily proportional to the amount of energy dissipated (Fig. 2b–c). This non-proportionality is a general property of quasistatically-driven disordered systems (Ortín & Goicoechea, 1998). Increasing the distribution width σ_{p_c}/p_c^0 by a factor of 20 (from 0.026 to 0.510) increases the slope of $|\Psi^{t-1\to t}|$ vs. $|S_w^{*,t} - S_w^{*,t-1}|$ by ~ 50. Here, $p_c = p_c^0 + \delta p_c$, where $p_c^0 = 2\gamma\cos\theta/b_0$ and $\delta p_c = p_c^0(\delta b/b_0)/(1 - \delta b/b_0)$. The slope was found by fitting a straight line (in dashed gray) to the conditional average of the data (solid black line in insets of Fig. 2b–c). The larger slope reflects the increased dissipation per avalanche size, due to the depinning from the stronger defects. We note the larger spread as well as deviation from a linear fit of smaller values, emphasized in log-log plots (Fig. 2b–c insets).

Next, we examine how the system properties affect the total dissipation along a closed drainage-imbibition cycle, Ψ_{cyc}. We find that Ψ_{cyc} scales with the disorder strength σ_{p_c}; for the Gaussian distributions studied here, $\Psi_{\text{cyc}} \sim (\sigma_{p_c})^n$ with $n \approx 1.4$ (Fig. 3a). This nonlinear relationship is a result of interactions among the heterogeneities due to the lateral correlation caused by interfacial tension (Holtzman et al., 2020). Dissipation is also controlled by the effective gravity g_e which sets the Bond number, namely the ratio of gravitational to capillary forces. Increasing g_e reduces the capillary rise (Jurin's height), restricting the size of the avalanches $|S_w^{*,t} - S_w^{*,t-1}|$ and hence the dissipated energy, cf. Fig. 3b and Videos 3–4 in Supporting Information.

4 Experiments exposing viscous dissipation and the limitation of the quasi-static concept

The simulations above provide a quantitative analysis of the energy losses associated with the dissipation of interfacial energy (stored in the deformed interface configurations (Morrow, 1970)) in ideally quasistatic conditions. The simulated PS trajectories show good agreement with an experiment in a disordered Hele-Shaw cell with similar material and geometrical properties, as shown in Fig. 4. The experimental setup, procedure and

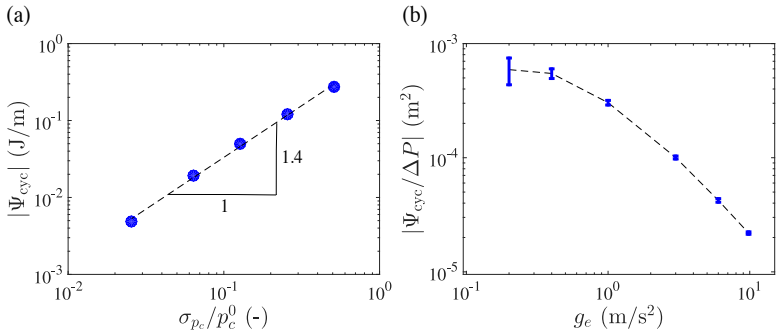

Figure 3. Impact of system properties on the energy dissipated in closed PS cycles, $\Psi_{\rm cyc}$: (a) Nonlinear scaling with the defect strength distribution σ_{p_c}/p_c^0 (dashed line); (b) Dissipation decreases with effective gravity g_e. To compensate for differences in the required driving force, $\Psi_{\rm cyc}$ is normalized by the width in pressure of the hysteresis cycle, ΔP. Each point is an average over 5 disorder realizations (15 for $g_e = 0.2$ m/s^2); error bars show the standard deviation.

analysis are detailed in the Supporting Information. For the specific set of parameters in Fig. 4 (dichotomic gap spacing $b_0 = 0.46(1)$ mm and $\delta b = 0.06(1)$ μm, disorder units of size $0.40(1) \times 0.40(1)$ mm^2 covering 35% of the total area, and $g_e = 0.86(1)$ m/s^2, see Supporting Information), the dissipated energy computed from the area enclosed within the PS cycle in the experiments is larger only by ∼18% than in the simulations. This implies that capillary losses account for most of the energy dissipated in quasistatic fluid displacements. Moreover, the primary imbibition curve and the early stages of subsequent drainage agree well, but the experimental data depart from the simulated drainage curve as the external pressure is lowered further. This also produces a small shift in the internal cycle. The lower external pressure required to drain a given wet area in the experiments, corresponding to a larger external work, is responsible for the larger dissipation measured experimentally. We note that since our external forcing P (or H) is in the wetting fluid, it is of opposite sign to the capillary pressure; thus, in our representation drainage occurs at lower P than imbibition, in contrast with the conventional capillary pressure curve.

Another interesting feature in Fig. 4 is the behavior of the inner cycle. While the numerical simulations display perfect return-point memory (as proved in Holtzman et al. (2020)), the experimental inner cycle does not rejoin the primary drainage curve at the same point exactly. This is due to the larger steps of driving pressure (P or H) in the experiments (Fig. S1 in Supporting Information), deviating from the infinitesimal perturbations required in the quasistatic case, that could be realized numerically but not experimentally; this was confirmed by simulating coarser H increments.

5 Discussion

Our results indicate that the interfacial energy dissipated in Haines jumps accounts for most of the energy dissipated in slowly driven systems (e.g. as acoustic emissions (Moebius & Or, 2012)), in agreement with observations from experiments driven at constant rate (Berg et al., 2013; Hu et al., 2018; Måløy et al., 2021). For the experiment presented in this paper, our quasistatic approach accounts for ∼80% of the energy dissipated during fluid displacements (Fig. 4). We argue that the remaining ∼20% discrepancy originates from viscous dissipation caused by a finite velocity of the wetting fluid in experiments vs. the zero velocity considered in the model. A nonzero velocity is an inherent feature of Haines jumps (rheons), regardless of how slow the interface is driven (Berg et al., 2013). Moreover, the corresponding viscous pressure drop depends on the sign of the front velocity, and thus plays opposite roles in drainage and imbibition. A small asymmetry between imbibition and drainage was already observed in experiments of slow displacements through a localized constriction (single defect) (Planet et al., 2020); this asymmetry accumulates and intensifies in a disordered medium composed of multiple defects where deformations take place cooperatively as Haines jumps. The role of viscous dissipation in imbibition-drainage cycles at finite flow rate, and its impact on the property of return point memory is the subject of ongoing research.

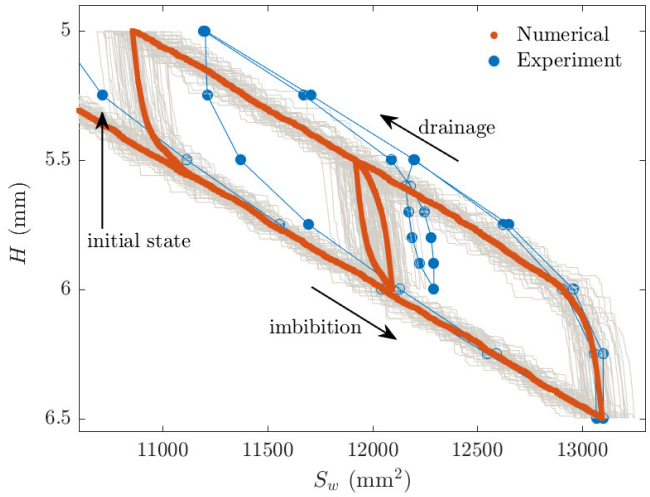

Figure 4. Simulated and experimental PS cycles in terms of external head H and wet area S_w in the imperfect Hele-Shaw cell shown in Fig. 1, using the same defect statistics. The numerical curve is the result of averaging 52 independent realizations (in gray). The uncertainty of the experimental data (single experiment) is smaller than the symbol size.

Another source of disparity between our model and quasistatically-driven experiments is the long relaxation timescale required for the interface to attain mechanical equilibrium at a new Jurin's height after each small pressure step (Clotet et al., 2012; Schlüter et al., 2017). In fact, the interface may continue to experience fluctuations even after reaching the Jurin's height (Lago & Araujo, 2001; Shikhmurzaev & Sprittles, 2012). Hence, the seemingly reversible, non-dissipative displacements (isons) also contribute to viscous dissipation, though to a lesser extent than Haines jumps (rheons). Additional mechanisms that can cause hysteresis and dissipation such as dynamic wetting, snap-off, and fluid trapping (Bonn et al., 2009; Moebius & Or, 2012; Moebius et al., 2012; Giacomello et al., 2016) are not considered in our model, which is characterized by a single continuous, univalued interface.

In conclusion, we have derived a thermodynamic framework that allows the quantification of energy dissipated via Haines jumps in capillary pressure-saturation trajectories at continuum scale from the microscopic mechanisms of surface tension and capillarity. The analysis presented here applies in fact to all modeling approaches displaying return-point memory for which the internal energy of multiphase configurations is a true state function. Relevant examples include the compartmental models introduced in Refs. (Cueto-Felgueroso & Juanes, 2016) and (Helland et al., 2021). Return-point memory appears therefore as a very useful property to extend classical equilibrium thermodynamic principles to nonequilibrium systems driven through metastable equilibria. The present approach provides in this way a means of upscaling fluid-fluid displacements in disordered media, and a generic method of potential interest in quasistatically-driven disordered systems.

References

Albers, B. (2014). Modeling the hysteretic behavior of the capillary pressure in partially saturated porous media: A review. *Acta Mech.*, *225*, 2163–2189. doi: 10.1007/s00707-014-1122-4

Alvine, K. J., Shpyrko, O. G., Pershan, P. S., Shin, K., & Russell, T. P. (2006). Capillary filling of anodized alumina nanopore arrays. *Phys. Rev. Lett.*, *97*(17), 175503. doi: 10.1103/PhysRevLett.97.175503

Ayaz, M., Toussaint, R., Schäfer, G., & Måløy, K. J. (2020). Gravitational and finite-size effects on pressure saturation curves during drainage. *Water Resources Research*, *56*(10), e2019WR026279.

Bedeaux, D., & Kjelstrup, S. (2022). Fluctuation-dissipation theorems for multiphase flow in porous media. *Entropy*, *24*(1). doi: 10.3390/e24010046

Berg, S., Ott, H., Klapp, S. A., Schwing, A., Neiteler, R., Brussee, N., ... Stampanoni, M. (2013). Real-time 3D imaging of Haines jumps in porous media flow. *P. Natl. Acad. Sci. USA*, *110*(10), 3755–3759.

doi: 10.1073/pnas.1221373110

Bertotti, G., & Mayergoyz, I. D. (Eds.). (2006). *The science of hysteresis, vol. 1: Mathematical modeling and applications*. Academic Press.

Bonn, D., Eggers, J., Indekeu, J., Meunier, J., & Rolley, E. (2009, may). Wetting and spreading. *Rev. Mod. Phys.*, *81*(2), 739–805. doi: 10.1103/RevModPhys.81.739

Clotet, X., Planet, R., & Ortín, J. (2012). Capillary rise in Hele-Shaw models of disordered media. *J. Colloid Interface Sci.*, *377*(1), 387-395. doi: 10.1016/j.jcis.2011.12.080

Cueto-Felgueroso, L., & Juanes, R. (2016). A discrete-domain description of multiphase flow in porous media: Rugged energy landscapes and the origin of hysteresis. *Geophys. Res. Lett.*, *43*(4), 1615-1622. doi: 10.1002/2015GL067015

Denisov, D., Lörincz, K., Uhl, J., Dahmen, K., & Schall, P. (2016). Universality of slip avalanches in flowing granular matter. *Nat. Commun.*, *7*(1), 1–6.

Ganesan, V., & Brenner, H. (1998). Dynamics of two-phase fluid interfaces in random porous media. *Phys. Rev. Lett.*, *81*(3), 578–581. doi: 10.1103/PhysRevLett.81.578

Giacomello, A., Schimmele, L., & Dietrich, S. (2016). Wetting hysteresis induced by nanodefects. *P. Natl. Acad. Sci. USA*, *113*(3), E262–E271. doi: 10.1073/pnas.1513942113

Grinstein, G., & Ma, S.-k. (1983). Surface tension, roughening, and lower critical dimension in the random-field ising model. *Phys. Rev. B*, *28*, 2588–2601. doi: 10.1103/PhysRevB.28.2588

Helland, J. O., Jettestuen, E., & Friis, H. A. (2021). A discrete-domain approach to three-phase hysteresis in porous media. *Water Resour. Res.*, *57*(6), e2021WR029560. doi: https://doi.org/10.1029/2021WR029560

Hiratsuka, T., Tanaka, H., & Miyahara, M. T. (2016). Critical energy barrier for capillary condensation in mesopores: Hysteresis and reversibility. *J. Chem. Phys.*, *144*(16).

Holbrook, N. M., & Zwieniecki, M. A. (2008). Transporting water to the tops of trees. *Phys. Today*, *61*(1), 76-77. doi: 10.1063/1.2835167

Holtzman, R., Dentz, M., Planet, R., & Ortín, J. (2020). The origin of hysteresis and memory of two-phase flow in disordered media. *Commun. Phys.*, *3*, 222.

Hu, R., Wu, D. S., Yang, Z., & Chen, Y. F. (2018). Energy Conversion Reveals Regime Transition of Imbibition in a Rough Fracture. *Geophys. Res. Lett.*, *45*(17), 8993–9002. doi: 10.1029/2018GL079302

Jensen, H. J. (1998). Self-organized criticality: Emergent complex behavior in physical and biological systems. Cambridge University Press.

Keim, N. C., Paulsen, J. D., Zeravcic, Z., Sastry, S., & Nagel, S. R. (2019). Memory formation in matter. *Rev. Mod. Phys.*, *91*, 035002. doi: 10.1103/RevModPhys.91.035002

Kierlik, E., Monson, P. A., Rosinberg, M. L., Sarkisov, L., & Tarjus, G. (2001). Capillary condensation in disordered porous materials: Hysteresis versus equilibrium behavior. *Phys. Rev. Lett.*, *87*(5), 055701. doi: 10.1103/PhysRevLett.87.055701

Lago, M., & Araujo, M. (2001). Capillary rise in porous media. *J. Colloid Interface Sci.*, *234*(1), 35-43. doi: https://doi.org/10.1006/jcis.2000.7241

Leschhorn, H., Nattermann, T., Stepanow, S., & Tang, L. H. (1997). Driven interface depinning in a disordered medium. *Annalen der Physik (Leipzig)*, *6*(1), 1–34. doi: 10.1002/andp.19975090102

McClure, J. E., Berg, S., & Armstrong, R. T. (2021). Thermodynamics of fluctuations based on time-and-space averages. *Phys. Rev. E*, *104*, 035106. doi: 10.1103/PhysRevE.104.035106

Moebius, F., Canone, D., & Or, D. (2012). Characteristics of acoustic emissions induced by fluid front displacement in porous media. *Water Resour. Res*, *48*(11), 1–12. doi: 10.1029/2012WR012525

Moebius, F., & Or, D. (2012). Interfacial jumps and pressure bursts during fluid displacement in interacting irregular capillaries. *J. Colloid Interf. Sci.*, *377*(1), 406–415. doi: 10.1016/j.jcis.2012.03.070

Morrow, N. (1970). Physics and thermodynamics of capillary action in porous media. *Ind. Eng. Chem. Res.*, *62*, 32-56.

Måløy, K. J., Moura, M., Hansen, A., Flekkøy, E. G., & Toussaint, R. (2021). Burst dynamics, up-scaling and dissipation of slow drainage in porous media. *Front. Phys.*, *9*. doi: 10.3389/fphy.2021.796019

Ortín, J., & Goicoechea, J. (1998). Dissipation in quasistatically driven disordered systems. *Phys. Rev. B*, *58*(9), 5628–5631. doi: 10.1103/PhysRevB.58.5628

Pashine, N., Hexner, D., Liu, A. J., & Nagel, S. R. (2019). Directed aging, memory, and nature's greed. *Sci. Adv.*, *5*(12), 1–8. doi: 10.1126/sciadv.aax4215

Planet, R., Díaz-Piola, L., & Ortín, J. (2020). Capillary jumps of fluid-fluid fronts across an elementary constriction in a model open fracture. *Phys. Rev. Fluids*, *5*, 044002. doi: 10.1103/PhysRevFluids.5

.044002
Primkulov, B. K., Chui, J. Y. Y., Pahlavan, A. A., MacMinn, C. W., & Juanes, R. (2020). Characterizing dissipation in fluid-fluid displacement using constant-rate spontaneous imbibition. *Phys. Rev. Lett.*, *125*, 174503. doi: 10.1103/PhysRevLett.125.174503
Pruessner, G. (2012). Self-organised criticality: Theory, models and characterisation. Cambridge University Press.
Sahimi, M. (2011). *Flow and transport in porous media and fractured rock.* N.Y.: Wiley VCH Verlag GmbH.
Schlüter, S., Berg, S., Li, T., Vogel, H.-J., & Wildenschild, D. (2017). Time scales of relaxation dynamics during transient conditions in two-phase flow. *Water Resour. Res*, *53*(6), 4709-4724. doi: https://doi.org/10.1002/2016WR019815
Shikhmurzaev, Y. D., & Sprittles, J. E. (2012). Anomalous dynamics of capillary rise in porous media. *Phys. Rev. E*, *86*, 016306. doi: 10.1103/PhysRevE.86.016306
Shohat, D., & Lahini, Y. (2023). Dissipation indicates memory formation in driven disordered systems. *Phys. Rev. Lett.*, *130*, 048202. doi: 10.1103/PhysRevLett.130.048202
Sornette, A., & Sornette, D. (1989). Self-organized criticality and earthquakes. *EPL*, *9*(3), 197–202. doi: 10.1209/0295-5075/9/3/002
Tranter, T., Gostick, J., Burns, A., & Gale, W. (2018). Capillary hysteresis in neutrally wettable fibrous media: a pore network study of a fuel cell electrode. *Transp. Porous Media*, *121*(3), 597–620.
Valiullin, R., Naumov, S., Galvosas, P., & Al., E. (2006). Exploration of molecular dynamics during transient sorption of fluid in mesoporous materials. *Nature*, *443*, 965–968. doi: https://doi-org.sire.ub.edu/10.1038/nature05183
Wiese, K. J. (2022). Theory and experiments for disordered elastic manifolds, depinning, avalanches, and sandpiles. *Rep. Prog. Phys.*, *85*(8), 086502. doi: 10.1088/1361-6633/ac4648

Open Research Section

All data used to generate the figures and conclusions in the paper can be downloaded from: `https://dx.doi.org/10.6084/m9.figshare.22623262`.

Acknowledgments
We acknowledge J. Canadell for his help with the experiments. RH acknowledges support from the Engineering and Physical Sciences Research Council (EP/V050613/1); MD and JO received support from the Spanish Ministry of Science and Innovation through the project HydroPore (PID2019-106887GB-C31 and C32); RP and JO were also supported by AGAUR (Generalitat de Catalunya) through grant 2021-SGR-00450.

Supporting Information for "The relation between dissipation and memory in two-fluid displacements in disordered media"

Ran Holtzman,[1] Marco Dentz,[2] Ramon Planet,[3,4] and Jordi Ortín[3,4]

[1] *Coventry University, Centre for Fluid and Complex Systems, Coventry, United Kingdom**

[2] *Spanish National Research Council (CSIC), Barcelona, Spain*

[3] *Departament de Física de la Matèria Condensada, Universitat de Barcelona, Martí i Franquès 1, 08028 Barcelona, Spain*

[4] *Universitat de Barcelona Institute of Complex Systems, Barcelona, Spain*

I. NUMERICAL IMPLEMENTATION OF THE QUASI-STATIC MODEL

We use a finite differences discretization of the interface in the x direction into equally-spaced cells of size Δx, to obtain the force balance at a given equilibrium configuration t, Eq. (5)

$$p_e(x_i) = \frac{\gamma\left(h_{i+1} + h_{i-1} - 2h_i\right)}{\Delta x^2} - \rho g_e h_i + P + p_c(x_i, h_i), \tag{S1}$$

where $h_i = h(x_i)$. This provides the corresponding expressions for the work (Eq. (2))

$$W^{(t-1)\to t} = P^t \Delta x \sum_{i=1}^{N} [h_i^t - h_i^{t-1}], \tag{S2}$$

and the internal energy (Eq. (7))

$$U^t = \Delta x \sum_{i=1}^{N} \left\{ \frac{\gamma}{2} \left[\frac{h_{i+1}^t - h_{i-1}^t}{2\Delta x} \right]^2 + \frac{1}{2}\rho g_e (h_i^t)^2 - \Phi_0^{h_i^t} \right\}. \tag{S3}$$

For the first term in Eq. (7), we use the periodic boundary conditions, $h_0 = h_N$ and $h_{N+1} = h_1$, to evaluate the derivatives at the domain edges. The second and third terms arise from integrating from 0 to $h(x)$. Unlike other terms, $\Phi_0^{h_i^t}$ cannot be computed analytically, because of the nonlinear, non-monotonic dependence of p_c on both x and y, such that during an avalanche between two consecutive configurations the interface can change from being on a defect to leaving it and vice versa. Thus, $\Phi_0^{h_i^t}$ is evaluated numerically using a fine discretization in y, breaking each single avalanche (between t and $t-1$) into many smaller "substeps" which correspond to non-equilibrium configurations that our model does not resolve. Using $p_c = p_c^0 + \delta p_c$, we express this term as a sum of integrals: $\Phi_0^{h_i^t} = \int_0^{h_i^t} dy\ p_c^0 + \int_0^{h_i^t} dy\ \delta p_c(x_i, y)$. With p_c^0 being a constant, the first is simply equal to $p_c^0 h_i^t$. The second is evaluated by summation over all substeps from $j = 1$ (when the interface is at the cell inlet $y = 0$, i.e. $t = 0$) to $J = \mathrm{int}(h_i^t/\Delta y)$ (current configuration t): $\int_0^{h_i^t} dy\ \delta p_c(x_i, y) = \Delta y \sum_{j=1}^{J} (\delta p_c)_{i,j}$. Here j is the discretization in y, and $(\delta p_c)_{i,j}$ is zero unless the interface at $y = j\Delta y$ is on a defect.

We note that the discretization of Eq. (5) as well as the finite accuracy with which we resolve the interface configuration $h(x)$ (denoted ϵ in [1]) are a source of difference between the computed work $W^{t-1\to t}$ and internal energy $U^t - U^{t-1}$, manifested as numerical dissipation. We correct this by filtering out all the values of $\Psi^{t-1\to t}$ which fall below a threshold Ψ_{num} computed analytically from the difference between $U^t - U^{t-1}$ and $W^{t-1\to t}$ during advancement of an undeformed (flat) interface.

The simulations presented in the paper are using the following parameters (see [1] for complete description of parameters): (a) material properties of surface tension $\gamma = 20.7$ mN/m; gravitational acceleration $g = 9.81$ m/s^2, and oil density $\rho = 998$ kg/m^3 (considering oil and air as wetting and non-wetting fluids) with vanishing static contact angle (considering perfect wettability of the oil); (b) setup using $b_0 = 0.46$ mm; $\alpha = 2^o21'$ ($g_e = 0.4018$ m/s^2; incremental changes of external forcing $\Delta H = 0.05$ mm. and (c) numerical resolution of $\Delta x = 0.1$ mm; $J = 1000$ substeps. For simulations with disorder (Figs. 2–4) we used defects of size 4×4 units, randomly populated in space with occupancy $\psi = 0.35$ (defects covering 35% of the cell area).

Case-specific settings include: (i) Fig. 2 and Fig. 3a: sample size of 800×800 units ($L_x = L_y = 80$ mm), with δp_c for each unit being a random variable statistically independent of the others and drawn from a Gaussian distribution centered around zero; numerical accuracy of $\delta h = 5 \times 10^{-6}$ mm and $\epsilon = 0.01$ Pa. (ii) Fig. 3b: $L_x = 400$ and $L_y = 600$ units, $\delta b = 0.06$ mm averaging over 15 realizations for $g_e = 0.2$ m/s^2 and 5 realizations for the other g_e values (due to the increased sensitivity

* ran.holtzman@coventry.ac.uk

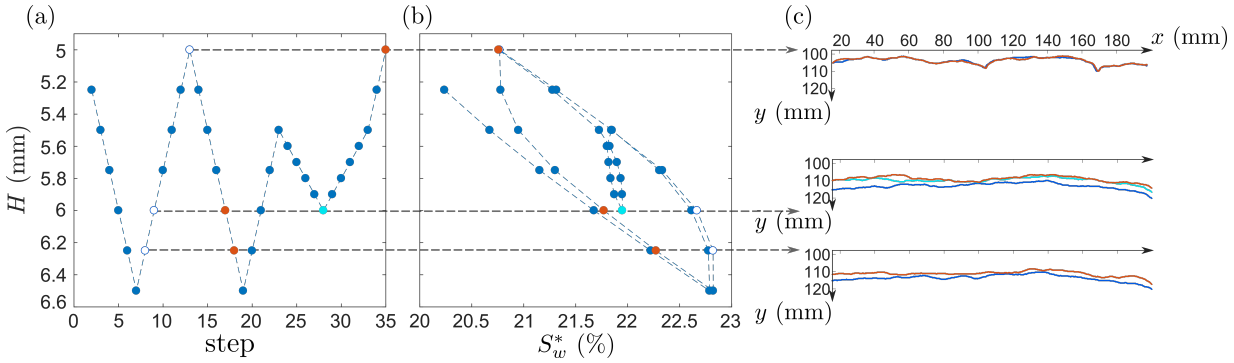

FIG. S1. (a) The experimental protocol is a sequence of 35 equilibrium configurations reached by setting the external head, H (see Fig. 1). The initial state is reached by performing an imbibition displacement from the cell inlet. From there on, several major and minor imbibition–drainage cycles are carried out between preselected values of the driving pressure. To approach the condition of quasistatic driving, the steps in pressure head were as small as of $|\Delta H| = 0.25(1)$ mm (0.10(1) mm in the inner cycle), separated by time intervals of 5 min (2 min in the inner cycle). (b) The corresponding pressure-saturation trajectories (also plotted in Fig. 4 in the main text; here saturation is presented in dimensionless form, i.e. wetted area per total cell area, S_w^*). The inner cycle performed in the middle of the second drainage displacement shows that return-point memory is not perfectly achieved in this experiment. However, the red point of lower H ($H \simeq 5.0$ mm) is nearly the same in the two drainage curves (with and without inner cycles), demonstrating that the memory of previous displacements is erased when internal cycles are completed (the so-called "wiping out" property). (c) The corresponding interface configurations for each of the 3 highlighted values of external head H, using matching colors, demonstrate multivaluedness—that different configurations can be reached at the same applied external forcing depending on the previous displacement history. Notice also the striking similarity of the two-phase configurations at lowest H (5.0 mm), resulting from wiping out the memory of the internal cycle. Here, y is measured from the cell inlet.

to details of individual realizations at lower g_e); $\delta h = 2.5 \times 10^{-6}$ mm; $\epsilon = 0.005$ Pa. (iii) Fig. 4: averaging over 52 realizations, cell size of $L_x = 600$ and $L_y = 250$ units, dichotomic distribution of defect strength, $\alpha = 5°3'$ such that $g_e = 0.9$ m/s^2. $\Delta H = 4.4 \times 10^{-4}$ mm; $\delta h = 8.8 \times 10^{-7}$ mm; $\epsilon = 0.0018$ Pa. Using $L_x = 60$ mm (600 units) was found sufficient to provide statistically representative average, closely matching a more computationally intensive simulation with $L_x = 190$ mm (the experimental system size) while providing a smoother pressure-saturation (PS) trajectory (averaging over the details of specific realization).

II. EXPERIMENTAL PS CYCLE IN A DISORDERED MEDIUM

The disordered medium in the experiments reported in Fig. 4 in the main text is a Hele-Shaw cell made of two parallel glass plates of size 190×500 mm^2 separated by a narrow gap. The gap spacing b is randomly distributed in space from a dichotomic distribution ($b_0 = 0.46(1)$ mm, with δb being 0 or 0.06(1) mm), using $0.40(1) \times 0.40(1)$ mm non-overlapping square copper patches deposited on a fiberglass board, covering 35% of the total area. The cell is tilted by an angle $\alpha = 5°3'(2')$ providing an effective gravity of $g_e = 0.86(1)$ m/s^2, to prevent the formation of viscous fingers during slow drainage (Fig. 1).

Note that thickness variations in the experimental cell are small compared to the average gap thickness, and thus have a negligible impact on integral quantities. The volume of the wetting phase in the cell is well approximated by $V_w = b_0 S_w$, and the (dimensionless) wetting-phase saturation is simply $S_w^* = S_w/(L_x \times L_y)$.

Before the experiment we wet the cell with a thin layer of oil to minimize the influence of previous displacements and wetting heterogeneities. Pre-wetting ensures also that the fluid wets perfectly (with vanishing contact angle) all the surfaces. The cell, initially filled with air, is invaded by silicone oil (Rhodorsil 47 V) of kinematic viscosity $\nu = 50$ mm/s^2, density $\rho = 998$ kg/m^3, and oil-air surface tension $\sigma = 20.7$ mN/m at room temperature. The oil invades the Hele-Shaw cell with a constant pressure at the inlet set by an oil container with controllable level H.

The experimental procedure is the following (for further details see Fig. S1): (i) we set $H = 5.00(1)$ mm and let oil invade the cell; (ii) once the interface is stabilized, we increment (in imbibition; decrement in drainage) the external pressure with steps of $\Delta H = 0.25(1)$ mm (0.10(1) mm for the inner cycle), waiting for 5 minutes (2 minutes for the inner cycle) between consecutive steps to reach a quasi-stationary state. The evolution of the oil-air interface is monitored using a digital camera with a resolution of 0.24 mm/pixel. We note however that the timescale for nearly complete arrest of the interface following a finite step in H is expected to be much larger than minutes [2–5], technically challenging the experimental realization of quasi-static driving.

Experimentally, mapping the position of the interface

to the specific location in the sample is also challenging. Such mapping is needed to obtain a direct comparison between simulations and experiments for identical microstructure. Instead, in Fig. 4 in the main text we compare the experimental data with an ensemble average of 52 simulations using statistically similar microstructure (dichotomic distribution). Averaging over realizations reduces the sensitivity to the specific details of a single realization (i.e. spatial location of defects), smoothing the PS curve.

III. CAPTIONS FOR MOVIES S1 TO S4

Movie S1: Dissipation in a medium with weak disorder.

Numerical simulations of an imbibition-drainage cycle in a disordered medium with a narrow defect strength distribution ($\sigma_{p_c}/p_c^0 = 0.026$), i.e. relatively homogeneous. Panels show the evolution of the interface configuration, pressure-saturation (PS), and the energy dissipated at each step as well as cumulative (since simulations started). Since the strength of the defects is relatively small, the hysteresis cycle is narrow, the interface experiences small deformations (small avalanches), and the energy dissipated during these jumps is relatively small (compare with the wide defect strength distribution of $\sigma_{p_c}/p_c^0 = 0.510$ in Movie S2). Note the wide range of magnitudes of dissipation events, where most of the dissipation during the cycle occurs in a handful of large events. Data is from the same simulation presented in Fig. 2b in the main paper.

Movie S2: Dissipation in a medium with strong disorder.

Numerical simulations of an imbibition-drainage cycle in a disordered medium with a wide defect strength distribution ($\sigma_{p_c}/p_c^0 = 0.510$), namely highly heterogeneous. Panels show the evolution of the interface configuration, pressure-saturation, and the energy dissipated at each step as well as cumulative (since simulations started). Due to the wide distribution, the strength of some of the defects is very high, leading to a wide hysteresis cycle, large interface deformations (large avalanches), and substantial energy dissipation during these jumps (compare with the narrow defect strength distribution of $\sigma_{p_c}/p_c^0 = 0.026$ in Movie S1). Note the wide range of magnitudes of dissipation events, where most of the dissipation during the cycle occurs in a handful of large events. Data is from the same simulation presented in Fig. 2c in the main paper.

Movie S3: Dissipation in a disordered medium under small gravity.

Numerical simulations of an imbibition-drainage cycle in a disordered medium at small gravity ($g_e = 0.2$ m/s^2, i.e. a nearly-flat cell tilted at an angle $\alpha = 1.2°$). Panels show the evolution of the interface configuration, pressure-saturation, and the energy dissipated at each step as well as cumulative (since simulations started). Since in the settings considered in this study gravity acts to stabilize the interface, low gravity corresponds to a large characteristic Jurin's height which allows for large avalanches in terms of both saturation changes and dissipation. Consequently, the PS cycle exhibits substantial hysteresis (wide cycle), where the jagged trajectory is composed of a few very large jumps in which most of the dissipation occurs. The magnitude of these events as well as of the overall amount of energy dissipated in the cycle is orders of magnitude larger than the case of high gravity (Movie S4). Data is from one of the simulations used to generate the ensemble average for $g_e = 0.2$ m/s^2 in Fig. 3b in the main paper.

Movie S4: Dissipation in a disordered medium under large gravity.

Numerical simulations of an imbibition-drainage cycle in a disordered medium at large gravity $g_e = 9.81$ m/s^2, i.e. a vertical cell tilted at an angle $\alpha = 90°$. Panels show the evolution of the interface configuration, pressure-saturation, and the energy dissipated at each step as well as cumulative (since simulations started). Since in the settings considered in this study gravity acts to stabilize the interface, large gravity corresponds to a small characteristic Jurin's height which inhibits the size of the avalanches in terms of both saturation changes and dissipation. Consequently, the PS cycle exhibits slight hysteresis (narrow cycle), where the relatively smooth trajectory is composed of multiple small jumps which dissipate small amount of energy. The magnitude of these events as well as of the overall amount of energy dissipated in the cycle is orders of magnitude smaller than the case of low gravity (Movie S3). Data is from one of the simulations used to generate the ensemble average for $g_e = 9.81$ m/s^2 in Fig. 3b in the main paper.

Notes (all Movies): (1) settings and parameter values are listed in Section I above; and (2) saturation plotted is in dimensionless form, S_w^*.

SUPPLEMENTARY REFERENCES

[1] R. Holtzman, M. Dentz, R. Planet, and J. Ortín, The origin of hysteresis and memory of two-phase flow in disordered media, Commun. Phys. **3**, 222 (2020).

[2] M. Lago and M. Araujo, Capillary rise in porous media, J. Colloid Interface Sci. **234**, 35 (2001).

[3] Y. D. Shikhmurzaev and J. E. Sprittles, Anomalous dynamics of capillary rise in porous media, Phys. Rev. E **86**, 016306 (2012).

[4] X. Clotet, R. Planet, and J. Ortín, Capillary rise in Hele-Shaw models of disordered media, J. Colloid Interface Sci. **377**, 387 (2012).

[5] S. Schlüter, S. Berg, T. Li, H.-J. Vogel, and D. Wildenschild, Time scales of relaxation dynamics during transient conditions in two-phase flow, Water Resour. Res **53**, 4709 (2017).